

Cd²⁺ incorporation in small pores LEV/ERI intergrown zeolites: a multi-methodological study

Cametti, G.; Scheinost, A.; Churakov, S. V.;

Originally published:

December 2020

Microporous and Mesoporous Materials 313(2021), 110835

DOI: <https://doi.org/10.1016/j.micromeso.2020.110835>

Perma-Link to Publication Repository of HZDR:

<https://www.hzdr.de/publications/Publ-31700>

Release of the secondary publication
on the basis of the German Copyright Law § 38 Section 4.

CC BY-NC-ND

Cd²⁺ incorporation in small pores LEV/ERI intergrown zeolites: a multi-methodological study

G. Cametti*^a, A. C. Scheinost^{b,c}, S. V. Churakov^{a,d}

^a Institute of Geological Sciences, Baltzerstrasse 1+3, 3012 Bern, Switzerland

^b The Rossendorf Beamline at the European Synchrotron Radiation Facility (ESRF), Avenue des Martyrs 71, 38043 Grenoble, France

^c Helmholtz Zentrum Dresden Rossendorf, Institute of Resource Ecology, Bautzner Landstrasse 400, 01328 Dresden

^d Paul Scherrer Institut, Forschungstrasse 111, 5232 Villingen PSI, Switzerland

Abstract

Small pores zeolites are successfully employed as catalysts, sorbents and molecular sieves. Their physiochemical properties can be improved by modifying their extraframework (EF) cation content via ion exchange. In this study, we investigate the crystal structure of a Cd-exchanged levyne (**LEV**) intergrown with erionite (**ERI**) by combining Single Crystal X-ray Diffraction (SCXRD), Molecular Dynamic simulations (MD) and Extended X-ray Absorption Fine-Structure spectroscopy (EXAFS). Data obtained from the different techniques, consistently indicated that Cd²⁺ distribute in an almost ordered fashion in **LEV**. In contrast, strong disorder of the EF species (Cd²⁺ and H₂O) is observed in the **ERI** cavities. In the latter, Cd²⁺ form aqueous complexes that are more mobile in comparison to Cd²⁺ in **LEV**, where it bonds to H₂O and framework-oxygen atoms. The formation of Cd-clusters is excluded based on EXAFS analysis. Finally, to discriminate

between thermal and static disorder, we proposed a new approach based on a combined MD and geometry optimization analysis.

Keywords: levyne, Cd-LEV, XRD, EXAFS, MD simulations, zeolites

*Corresponding author:

Georgia Cametti

Email: georgia.cametti@geo.unibe.ch

1. Introduction

Small pores zeolites are crystalline materials with pore size between 0.30-0.45 nm [1]. The framework is mainly constituted by (SiO₄) and (AlO₄) tetrahedra. The latter build up pores with maximum aperture-window of eight-membered rings (8MR), which allow passage of small molecules only. In the past decades, more attention has been addressed to small pores zeolites compared to medium and large microporous zeolites, because of their advantageous use in catalytic processes such as exhaust cleaning, partial oxidation of methane and olefin generation [1].

At date, forty-four framework types (natural and synthetic) are classified as small pores zeolites or 8MR zeolites. Among them, levyne (**LEV**) and erionite (**ERI**) are two naturally occurring zeolites belonging to the so-called ABC-6 family [2]. Levyne is described in the trigonal space group R-3m [2,3]. Single six-membered rings (6mR) of tetrahedra are stacked along the c-axis (stacking sequence AABCCABBC), forming the *lev* cavity (pore descriptor 4⁹6⁵8³) and the double six-membered ring (D6R) cage (pore descriptor 4⁶6²). Two interconnected 8-membered ring channels run parallel to [100]. The distribution of the extraframework (EF) cations differs from

sample to sample, based on the chemical composition [5-7]. In general, the EF cations are located along the three-fold axis in the lev cavity whereas at RT no cations are found in the D6R cage. Similar to levyne, the erionite structure is constituted by 6mR of tetrahedra, but a different stacking sequence along the c-axis (AABAAC) originates from a different system of channels and cavities. In erionite, the alternation of *eri* cavities [4¹²6⁵8⁶] and cancrinite cages [4⁶6⁵] along c results in the hexagonal space group *P6₃/mmc* [3,8]. Due to their structural similarity, these two zeolites are often found as intergrown phases in nature [9-12]. Concerning the synthesis route, LEV microporous aluminosilicates are always synthesized with the use of an overall structure directing agent (OSDA) [1] whereas obtaining pure ERI (with TMA) is difficult because it is often intergrown with OFF [13]. In addition, a LEV/ERI intergrowth (SSZ-105) is also reported in the patent literature [14]. From an applicative point of view, levyne is mainly applied for separation and sorption whereas the main exploitation of ERI materials is in catalytic processes [1 and reference herein].

Ion exchange is the most used method to change and tune the physio-chemical properties of zeolites. In particular, a large number of studies has been dedicated to the investigation of zeolites (natural and synthetic) exchanged with transition metals (Cu, Zn, Ag, etc.). Among them, Cd⁺²-exchanged hydrated and dehydrated zeolite structures [15-20] were extensively investigated due to their attractive catalytic capacities [21-23]. Since the chemical reactivity depends on the type of cationic complexes, understanding the nature of the metal species (aquo complexes, charged clusters, etc.) and their interaction with the zeolitic framework represents a key point. Difficulties arise when these species are affected by high disorder that can hamper the exact determination of their coordination chemistry. In this case, the largely adopted X-ray based diffraction methods must be accompanied by other techniques able to probe the short range order of the species of

interest. In particular, experimental and theoretical methods such as X-ray absorption spectroscopy (XAS) and molecular dynamics (MD) simulations have been successfully used as complementary methods for the analysis of metal species inside zeolites [24-27].

Recently, we characterized from a structural and chemical point of view an Ag^{+1} -exchanged levyne intergrown with erionite [28,29]. Our results showed that Ag^{+1} replaced the original EF cations content in both zeolites. In Ag-levyne, Ag ions were strongly disordered at partially occupied sites and, even if the structure at RT maintained the R-3m space group, upon heating, it experienced a different dehydration path compared to the pristine material (i.e. levyne-Ca). In the same study, we were able to characterize the intergrown Ag-erionite. Ag^{+1} ions were located in the eri cavity. In contrast, K atoms, originally in the cancrinite cage, could not be exchanged.

In this study, we report a detailed investigation of the structural incorporation of Cd^{2+} into levyne intergrown with erionite. The aim was: i) to determine the coordination chemistry and location of Cd^{2+} species in the two zeolites; ii) understand the effect of the framework type (LEV and ERI) on the Cd^{2+} distribution; iii) conceive a theoretical approach able to describe the disorder of the EF species. To reach these goals, experimental techniques were coupled with theoretical computations. Bulk structural data were obtained by Single Crystal X-Ray Diffraction (SCXRD) whereas X-ray Absorption Fine Structure (XAFS) spectroscopy and Molecular Dynamics (MD) simulations were used to get an insight into the local environment of Cd^{2+} and H_2O location within the zeolitic channels.

Such approach allowed us to obtain detailed information on the EF cation locations and to compare the EF cations distribution with that previously reported for the other known cationic forms of levyne.

This kind of research is fundamental to exploit the potential application of the new porous phase. Several studies on metal-exchanged zeolites, have already demonstrated that even if the position of the EF cations has little influence on the RT structure, it plays a key role on the structural modifications occurring upon heating, leading to different dehydration paths and new porous phases.

2. Methods

2.1 Sample description

The pristine levyne sample was a levyne-Ca from Beech Creek, Oregon, U.S.A. (sample number A7827 of Natural History Museum of Bern) with chemical composition $\text{Ca}_{2.53}\text{Na}_{0.72}\text{K}_{0.23}(\text{Al}_{6.26}\text{Si}_{11.8}\text{O}_{36})\cdot 17.58 \text{ H}_2\text{O}$. The specimen was the same used in our previous studies [28,30] and consisted of levyne intergrown with erionite [28]. For the diffraction experiments a single fragment of each phase could be separated whereas the XAFS measurements were performed on powder (see section 2.6) consisting thus of both levyne and erionite.

2.2 Exchange experiments

The exchange experiments were performed in two steps: at first, small fragments (dimension between 100-400 μm) of natural levyne intergrown with erionite were put in an autoclave filled with 2M NaCl solution at 100°C for 4 weeks. The solution was renewed every three days. After that, the crystals were removed from the autoclave and washed with deionized water. This first step produced a partially exchanged Na-levyne, with residual Ca content non-homogeneously distributed in the crystals. In the second exchanged step, the partially Na-exchanged crystals were put in contact with 1 M $\text{Cd}(\text{CH}_3\text{COO})_2$ solution ($\text{pH} \approx 6$) for 4 weeks at 100°C. Similar to step 1,

the solution was renewed every three days. After the exchange experiments the crystals were washed with deionized water and the chemical composition was controlled by energy dispersive spectrometry (EDS) using a ZEISS EVO50 scanning electron microscope (SEM).

2.3 Chemical analyses

To determine the effect of the exchange process on both phases (i.e. levyne and erionite), chemical analyses were performed on different crystal fragments. The two zeolites could be distinguished based on the different crystal morphology, i.e. bulky for levyne and fibrous for erionite [28] (see results section). Operating conditions were 20 kV, accelerating voltage, 10 mm working distance, 30 s acquisition time. The chemical formula was calculated based on 36 (Si+Al) atoms after renormalization of the chemical analyses hypothesizing a water content of 18% wt. The reliability of the chemical analyses was evaluated by the charge balance error test [31].

2.4 Single Crystal X-ray Diffraction (SCXRD)

A single fragment of Cd-levyne with dimension 0.10 x 0.12 x 0.13 mm was glued on the tip of a glass fibre mounted on a goniometer head. Diffraction data were collected using a Synergy-S Rigaku diffractometer equipped with a dual micro-focused source and a Hypix detector. The AgK α ($\lambda = 0.56087 \text{ \AA}$) radiation was chosen to minimize the absorption of cadmium. Data were integrated and corrected for absorption by using CrysAlisPro 171.40.29a software package [32]. Structure solution by direct methods using Shelxt [33] indicated space group R-3m.

To determine the structure of the intergrown erionite, a smaller fragment (0.01 x 0.07 x 0.08 mm) was selected under a binocular microscope, glued on the tip of a glass fibre and mounted on a goniometer head. Due to the small size of the crystal, diffraction data were collected using the more brilliant CuK α ($\lambda = 1.54184 \text{ \AA}$) radiation available on the same diffractometer utilized for

Cd-levyne. The data were reduced and corrected for absorption using CrysAlisPro 171.40.29a [32]. The structure was solved by direct methods [33] in space group $P6_3/mmc$.

Structural refinements were carried out by using neutral atomic scattering factors by Shelxl [34]. Atomic labels and coordinates of the framework were the same reported in Cametti and Churakov, 2020 [28]. Extraframework cations and water molecules were located by difference Fourier maps and labelled according to the nomenclature used for levyne-Ca [30].

Crystal data and refinements parameters are reported in Table 1. All structural drawings were produced by VESTA software [35].

2.5 Molecular dynamics (MD) simulations

The MD simulations were run using the Cp2k software package [36]. The calculations were performed in NPT (constant temperature and pressure, and flexible unit cell) ensemble based on Density Functional Theory (DFT). The integration time of the equations of motion was 0.5 fs. The simulations temperature of MD was set to 77°C to prevent the glassy behaviour of PBE-H₂O [37]. The electron exchange and correlations were described by the Perdew-Burke-Erzerhof functional [38]. The Kohn-Sham orbitals were expanded using a linear combination of atom-centred Gaussian type orbital functions. A short range double- ζ valence polarized basis set was employed for each atom kind [39]. Dispersion correction was taken into account using the DFT+2D method [40].

System set up. The starting coordinates of the Cd-LEV structural model were taken from X-ray data. The EF cations were considered all Cd ions and located at the main occupied sites as retrieved from X-ray structural refinement. The number of water molecules was set according to the chemical composition, i.e. 6 H₂O per Cd²⁺ ion. A fully flexible supercell $2 \times 1 \times 1$, containing 18 Cd, 72 Si, 36 Al, 323 O, 216 H was used. The structure of Cd-erionite was simulated using a

flexible supercell $1 \times 1 \times 1.5$ containing 6 Cd, 3 K, 39 Si, 15 Al, 109 O, 37 H₂O. Starting coordinates were taken from X-ray data.

The data, for both structures, were collected from a 15 ps long trajectory followed by at least 6 ps pre-equilibration. Theoretical XAFs spectra were calculated for each Cd²⁺ position in the supercell using FEFF 8.40 software [41,42]. The Fermi energies and the scattering potential were evaluated self-consistently using a cluster radius of 4 Å. Because the structural disorder is taken into account in MD trajectories, the Debye-Waller factor was set to 0.0002 Å². The amplitude reduction factor (S_0) was set to 0.9. For Cd-levyne 136 consequent frames separated by 125 fs interval were used to calculate the average Extended X-ray Absorption Fine Structure (EXAFS) function. Similarly, 136 consequent snapshots separated by 100 fs interval were used for Cd-erionite.

To discriminate between the effect of temperature (the MD simulations were run at 77°C) and that of atomic disorder on the XAFS spectra, a sequence of geometry optimizations were run for each phase (Cd-LEV and Cd-ERI) using the following method: 1) the atomic coordinates and unit cell parameters were taken from 10 subsequent MD snapshots, in the range from 10 to 20 ps in steps of 1 ps; 2) geometry and cell optimization were run for each snapshot; 3) for each optimized structure (ten in total for Cd-LEV and Cd-ERI), a theoretical $k^3\chi(k)$ -weighted function was obtained by averaging the spectra calculated for each Cd²⁺ in the supercell. The Debye-Waller factor in this case was set to 0.002 Å². Finally, an average chi function was obtained for both Cd-LEV and Cd-ERI by averaging the ten spectra calculated in step 3.

2.6 X-ray Absorption Fine Structure Spectroscopy (XAFS)

XAFS data were collected at the Rossendorf Beamline [43] at the European Synchrotron Radiation Facility (ESRF) in Grenoble, France using a Si(111) double-crystal monochromator and two Pt-coated mirrors for collimation and suppression of higher-order harmonics. The sample was gently

grounded, homogeneously mixed with boron nitride and subsequently pressed to form a pellet. The latter was then covered with capton tape and inserted in a sample holder.

The sample was measured in transmission mode under cryogenic conditions (~ 15 K) to suppress thermal contributions to the Debye-Waller term, using a 13-element high-purity Ge solid-state detector (Canberra) with digital signal analysis (XIA Xmap). Five individual XAS scans were energy-calibrated against a simultaneously measured Cd foil (26711 eV), corrected for fluorescence dead time and averaged using SIXpack, while subsequent data reduction steps and shell fits were conducted using WinXAS [44,45].

Extended X-ray Absorption fine structure (EXAFS) analysis was performed by Fourier transforming $k^3\chi(k)$ -weighted function between 2 and 14.5 \AA^{-1} using a Kaiser-Bessel window function. Theoretical backscattering paths were calculated with FEFF8.2 [41,42] using the Cd-levyne structure model used for DFT calculations. The refinement of the obtained pseudo radial distribution function was carried out by a multishell fit approach. The amplitude factor S_0 was set to 0.9 and a global phase shift ΔE was fitted for all paths.

3. Results

The investigated sample is characterized by two intergrown mineral phases with two different chemical compositions: one with a bulky morphology, corresponding to levyne and the other with a fibrous-like morphology identified as erionite (Figure S1). The EDS-SEM analyses of the levyne fragments indicated that Cd completely replaced Na ions. However, residual calcium (varying from 0.39 to 0.7 apfu) was detected in all analytical points. In contrast, erionite fragments contained only K and Cd as extraframework cations (EF). Final chemical composition was

$\text{Cd}_{2.6}\text{Ca}_{0.6}\text{Al}_{6.6}\text{Si}_{11.4}\text{O}_{36}\cdot 18.0\text{H}_2\text{O}$ and $\text{Cd}_{2.2}\text{K}_{1.2}\text{Al}_{5.6}\text{Si}_{12.4}\text{O}_{36}\cdot 18\text{H}_2\text{O}$ for Cd-levyne and -erionite respectively.

3.1 Crystal structure of Cd-levyne. The structure of Cd-levyne maintained the R-3m space group characteristic of the natural levyne-Ca and of the Ag-exchanged one [28,30]. The unit cell volume was smaller than that reported for the pristine material and for Ag^{+1} -exchanged levyne, as expected by the smaller radius of Cd^{2+} compared to Ag^{1+} and Ca^{2+} .

According to the structural refinement (Table 2), most of cadmium ions are found at C1 (Occ. = 0.778(6)) and C5 (Occ. = 0.469(8)) sites. C3 site, refined with Ca scattering factors, is 50% occupied (Fig. 1a,b). The water molecules are located at four sites corresponding to W1, W2, W3, and W4 of the natural levyne-Ca.

C1 is coordinated by three H_2O at W1 ($d = 2.329(7)$ Å) and three framework-oxygen atoms at O2 ($d = 2.374(5)$ Å) whereas C5 is at the top of the *lev* cavity and bonds only to six framework oxygen at O5 ($d = 2.556(6)$ Å). C3 bonds to three H_2O at W2 ($2.764(16)$ Å) and three at W3 ($2.21(5)$ Å). Such short Ca-O distances are justified hypothesizing a partial occurrence of Cd^{2+} ions at this site: this is also suggested by the slightly higher Ca amount (1 apfu), obtained by the structural refinement, compared to that determined by the chemical analyses (0.6 apfu).

The structural parameters extrapolated from MD trajectories are consistent with those obtained by XRD data, indicating that the residual amount of Ca in the *lev* cavity has overall a negligible effect. In the theoretical structure, hypothesizing only Cd^{+2} ions as EF cations, Cd mainly locates at the top and bottom of the *lev* cavity (Fig. 2a), in correspondence of C1 and C5 sites. The local coordination environment of Cd^{2+} ions, which mainly bond to H_2O and framework oxygen of the D6R cage, also agrees with that determined by diffraction data (Fig. 2b). The analysis of the Cd-O bonds is reported in Fig. 2c. The radial distribution function (RDF) and corresponding

coordination number (CN) were calculated for Cd-O (O oxygen of the framework) and Cd-Ow (Ow water molecules) contacts. The Cd-Ow curve has a maximum at 2.28 Å whereas the Cd-O curve appears broader, with Cd-O distances mainly distributed between 2.32 and 2.43 Å. On average, each Cd is surrounded by two-framework oxygen atoms and three H₂O with distances between 2.2 and 2.5 Å.

3.2 Crystal structure of Cd-erionite. The structural parameters of Cd-erionite and corresponding relevant bond distances are reported in [Table 3](#) and [4](#), respectively. The space group *P6₃/mmc* is the same of that found for natural erionite [8].

In agreement with previous findings [46], the exchange process had no effect on K atoms, which remained in the cancrinite cage. Cadmium is found in the eri cavity, disordered at partially occupied sites. These positions are somewhat similar to those of the EF cations observed in Ag-exchanged erionite [28]. In particular, C1, C2 and C3 correspond to the sites with equivalent label in the structure of Ag-erionite. C1 (split in two subsites, C1 and C1A) is close to the wall of the six-membered ring window of the cancrinite cage. C2 (the most occupied site) and C2A are in the centre of the 6mR, at the top and bottom of the eri cavity. C3 is in the middle of the cavity, surrounded by two additional sites C4 and C4A (site symmetry 24l) which distributes in a ring-fashion, up and above C3 ([Fig. 3](#)). C4, C4A and C3 are low occupied (occupancy less than 0.10) and close to each other (distances 1.5-2.13), indicating a pronounced disorder of Cd²⁺ in the erionite cavity. The H₂O are also disordered at partially occupied sites, mainly in the 8mR window of the eri cavity and along the sixfold inversion-axis, bonded to C2. The strong disorder of the EF species may also justify the lack of approximately 25% of Cd atoms that could not be located by the structural refinement.

Such disordered configuration made difficult to interpret the exact coordination of Cd in erionite. In this specific case, we relied on the MD simulations. A snapshot of the arrangement of Cd and H₂O in the calculated structure is showed in Fig. 4a. In agreement with X-ray data, MD trajectories showed that Cd assumed diverse positions in each cavity. Cd ions in the centre of the eri cavity are displaced off the sixfold inversion-axis, toward the wall of the cavity. In addition, the Cd at the bottom and top of the cavity (C2, C2A sites in XRD refinement) are off from the centre of the 6mR.

The distribution of Cd-O distances (Fig. 4b) is similar to that obtained for Cd-levyne. Cd mainly bonds to H₂O, ca. 2 H₂O between 2.27 and 2.32 Å whereas the curve of Cd-O distances is significantly broad. The maximum of the RDF is found at 2.43 Å, where approximately only one framework oxygen atom is found.

3.3 Local environment of Cd²⁺

The $k^3\chi(\kappa)$ -weighted function and corresponding FT (uncorrected for phase shift) as obtained by standard EXAFS data reduction are reported in Fig. 5a,b. Note that the spectrum contains the proportional Cd contributions of both Cd-LEV and -ERI. The first peak at 1.8 Å was fitted by one Cd-O shell with Cd-O distance $R = 2.28$ Å and CN = 6. To properly fit the second peak at 1.9 Å different tests were performed using a single shell (Cd-Si or Cd-Ca) or a double-shell scheme (Cd-Si, Cd-Si or Cd-Si, Cd-Ca). The best fit was obtained with two Cd-Si shells at $R = 3.15$ Å and $R = 3.44$ Å, respectively (Table 5). Furthermore, an attempt was made to fit the small peak at 4.49 Å in the FT (Fig. 5b). According to XRD data, such broad peak at that distance is in agreement with the presence of K in the ERI phase. Nevertheless, a tentative fitting including the additional Cd-K scattering path was not successful and was not considered.

The Cd-O distances obtained from EXAFS analysis agree with those extrapolated by SC-XRD refinement and MD trajectories. The most occupied EF sites in Cd-levyne and Cd-erionite are C1 and C2, respectively. C1 in Cd-LEV bonds to W1 at 2.329(7) Å and C2 in Cd-ERI to W5 at 2.27(3) Å. Such distances are also in agreement with those reported by the MD trajectories, which indicated that, for both phases, the main peak of Cd-H₂O interactions is at 2.28 Å. The distances of the Cd-Si shell (Table 5) also match those of the simulated (Fig. 6) and refined structures. In Cd-LEV, similar distances are found between C5 and T2 sites (3.1781(17) Å) and C1 and T1 sites (3.4618(12) Å). Similarly, C2-T2 sites in Cd-ERI are at 3.216(1) Å.

4. Discussion

4.1 Static disorder and thermal motion

To try to unravel the contribution of each phase to the EXAFS spectrum, theoretical $k^3\chi(\kappa)$ -weighted chi function were calculated based on the MD trajectories for both Cd-LEV and Cd-ERI. Fig. 7a reports the experimental and the average theoretical chi function using a levyne/erionite ratio of 45:55. Such ratio, instead of 50:50 as reported in [29], was used to take into account the slight overestimation of Cd content in the simulated Cd-LEV structure (9 Cd vs 7.8 pfu calculated from chemical analysis). The theoretical spectra obtained from MD trajectories (of both Cd-LEV and Cd-ERI (Fig. S2)) at ambient conditions, substantially underestimate the intensities of the experimental $\kappa^3\chi(\kappa)$ functions collected at 15K (Fig. 7a). Two factors mainly influence the amplitude of the EXAFS- k^3 -weighted $\chi(\kappa)$ function: i) the coordination number and ii) the Debye-Waller factor. Since the structural models obtained from EXAFS-spectra fitting and MD are in good agreement and since the effect is more pronounced at high k values, it could be inferred that the mismatch of intensities is related to the thermal disorder. To mimic the low temperature conditions (low thermal disorder) and in the same time to account for the structural disorder, a set

of geometry optimisations was performed starting from the uncorrelated atomic configuration collected from MD simulations at ambient condition (as described in section 2.5).

By doing so, we expect to obtain a number of structural configurations with atoms confined to the local energy minima but representing structural disorder as it would be obtained for the geometry optimization in a very large supercell. In this approach MD trajectory is used to collect the thermally disorder structure, whereas geometry and cell optimisation brings the atoms towards the nearest local minima as expected to occur during the experimental measurement.

The theoretical EXAFS spectra were then collected for this set of geometry and cell optimised configurations. The EXAFS spectra obtained in such a way show a much better agreement with the experimental data (Fig. 7b). The slight shift toward lower κ values is also observed. An inspection of the $\kappa^3\text{-}\chi(\kappa)$ function of the single components (Cd-LEV and Cd-ERI) indicated that such shift is mainly caused by the LEV phase (green curve in Fig.S3). From a structural point of view, shorter κ values indicate longer absorber-scatterer distances; these discrepancies might be related to the presence of residual Ca or slightly different hydration shell [47].

4.2 Influence of the framework type on the disorder of the EF species

The results obtained by different techniques consistently showed that in Cd-LEV, Cd^{+2} ions distributed in a fairly ordered fashion within the pores. In particular, they mainly replace the cations at the most occupied crystallographic sites (i.e. C1, C3, and C5) present in levyne-Ca. In contrast, in Cd-ERI, the disorder is much more pronounced and no obvious parallelism can be drawn with the EF sites position of natural erionite [8]. The arrangement of cadmium in the erionite pores resemble that of silver in Ag-exchanged erionite [28], though strong differences appear in sites occupancy. For example, C1 site (occ. = 0.70), where most of Ag^{+1} ions are located in Ag-

ERI structure, is only 20% occupied in Cd-ERI. Cd ions are significantly more diffuse in erionite than in levyne, especially if the middle of the eri cavity is considered. Interestingly, the opposite situation is found in the Ag-exchanged forms, i.e. Ag ions are more diffuse and disordered in levyne respect to erionite [28]. It was suggested that the coordination chemistry of EF species in hydrated zeolites is close to that of aqueous solution chemistry [48]. Hence, the exchanged cations are in form of “aquo complexes that are mobile and only partially coordinated to framework oxygen in a dynamically disordered fashion” [48]. The same authors also pointed out that “the steric constraints imposed by” smaller pores “promote greater ligand dissociation during cation exchange” [48] which induces a greater interaction with the framework oxygen. Although the apertures and then the access to the respective zeolitic cavities is the same in LEV and ERI (i.e. 8MR), the eri cavity is significantly bigger than the lev one. Thus, the higher mobility of the most hydrated Cd ions in the eri cavity could be one cause of the greater disorder observed in Cd-ERI. The analysis of the Cd-OW distances distribution (Fig.2c and 4b) in Cd-LEV and Cd-ERI confirms that Cd²⁺ is “more hydrated” in erionite than in levyne, supporting our hypothesis. In levyne, Cd²⁺ coordinates to H₂O and framework oxygen and Cd¹⁺²(H₂O)₆ complexes do not form. In Cd-ERI, Cd ions in the middle of the eri cavity can be fully hydrated (and hence more mobile) (Fig.8a) or partially coordinated by framework oxygen atoms (Fig.8b).

4.3 Cationic clusters formation

The formation of cationic Cd_n^{m+} clusters into zeolites was first hypothesized based on Raman measurements [49] and reported for zeolite A [15,50,20]. Although in the structure of erionite the arrangement of C3 and C4 (Cd-Cd = 2.6 Å) resembles that of a cluster Cd₉⁸⁺ reported in the sodalite cage of zeolite A [20] we exclude the formation of metallic Cd, that is not supported by EXAFS analysis. Furthermore, our sample was measured at 15 K without previous dehydration neither by

thermal treatment nor by vacuum whereas Cd clusters reported in zeolite A were observed only on dehydrated samples.

5. Conclusions

The investigation of EF species in zeolites can be challenging when both H₂O and charge-compensating cations disorderly distribute in the pores. Although X-ray diffraction is one of the most used technique, different approaches are needed to properly characterize the position and coordination chemistry of the EF cations. In our study, by using a complementary experimental and theoretical approach, we could investigate in detail the Cd²⁺ arrangement in small pores zeolites, LEV and ERI. We found that, although the local environment of Cd²⁺ is similar in the two zeolites, differences in terms of disorder and coordination shell arise because of the different framework type (i.e. kind of cavities). Cd ions are octahedrally coordinate to H₂O and framework oxygen in LEV, and distribute in the lev cavity in an almost ordered manner. In contrast, even though Cd²⁺ partially coordinate to framework oxygen atoms, in Cd-ERI more mobile Cd(H₂O)₆ complexes are present in the middle of the eri cavity, leading to significant positional and dynamical disorder. High quality experimental EXAFS spectra and the molecular simulations allowed us to discriminate the effect of thermal and structural disorder in the measured and theoretically calculated XAS spectra based on the MD trajectories and structural geometry optimisation. This is a one of few examples of combined application of ab initio MD and experimental spectroscopy to a very complex chemical system in which the thermal and structural disorder could be discriminated.

Acknowledgements

We are thankful to Dr. Beda Hoffman of Natural History Museum of Bern who provided the levyné sample Beda Hoffman, sample. We acknowledge access to the Swiss National Supercomputing Center (CSCS) and UBELIX HPC cluster at the University of Bern. The Swiss National Science Foundation (SNF) is acknowledged for the Ambizione grant n. PZ00P2 173997 awarded to G. C. and for the R'Equip grant n. 206021_177033 awarded to P. Macchi.

CRedit author statement

Georgia Cametti: Conceptualization, Methodology, Investigation, Formal analysis, Writing-Original Draft. Andreas C. Scheinost: Investigation, Formal analysis, Writing - Review and Editing. Sergey Churakov: Methodology, Writing - Review and Editing.

References

- [1] M. Dusselier, M. E. Davis, *Chem. Rev.* 118 (2018) 5265-5329.
- [2] R. M. Barrer, I.S. Kerrer, *Trans. Faraday Soc.* 55 (1959) 1915-1923.
- [3] G. Gottardi, E. Galli, *Natural Zeolites*, vol. 18 Springer-Verlag, Berlin, 1985409.
- [4] S. Merlino, E. Galli, A. Alberti, *Tscher. Miner. Petrog.* 22 (1975) 117-129.
- [5] M. Sacerdoti, *Jb Neues Miner. Monat.* 3 (1996) 114-124.
- [6] G. D. Gatta, P. Comodi, P. Zanazzi, T. Boffa Ballaran, *Am. Mineral.* 90 (2005) 645-652.
- [7] P. Ballirano, G. Cametti, *Mineral. Mag.* 77 (7) (2013) 2887-2899.
- [8] A. Alberti, A. Martucci, E. Galli, G. Vezzalini, *Zeolites* 19 (1997) 349-352.
- [9] M. Shimazu, T. Mizota, *J. Jap. Ass. Mineral. Petr. Econ. Geo.* 67 (1972) 418-424.
- [10] J. M. Bennett, R. W. Grose, (1978) In: Sand L. B., Mumpton, F. A., (eds) *Natural Zeolites*. Pergamon, Oxford, pp 77-84.
- [11] S. W. Wise, R. W. Tschernich, *Am. Mineral.* 61 (1976) 853-863.
- [12] E. Passaglia, E. Galli, R. Rinaldi, *Contrib. Mineral. Petr.* 43 (1974) 253-259.
- [13] K. P. Lillerud, J. H. Raeder *Zeolites* 6 (1986) 474-483.
- [14] D. Xie, Lew C. M. US Patent 9663380 2017.
- [15] L. B. McCusker, K. Seff, *J. Am. Chem. Soc.* 101 (1979), 5235– 5239
- [16] S. B. Jang, U. S. Kim, Y. Kim, K. Seff, *J. Phys. Chem.* 98 (1994) 3796-3800.

- [17] Y. Lee, B. A. Reisner, J. C. Hanson, G. A. Jones, J. B. Parise, D. R. Corbin, B. H. Toby, A. Freitag, J. Z. Larese, *J. Phys. Chem B* 105 (2001) 7188-7199.
- [18] E. Y. Choi, S. H. Lee, Y. Kim, Y. W. Han, K. Seff, *J. Phys. Chem. B* 106 (2002) 7569–7573.
- [19] J. Wang, D. Wang, H. Zeng, Z. Zhou, *RSC Advances* 5 (2015) 77490-77494
- [20] J. E. Readman, P. D. Barker, I. Gameson, J. A. Hriljac, W. Zhou, P.P. Edwards, P. Anderson, *Chem. Commun.* (2004) 736-737.
- [21] G. Onyestyak, D. Kallo, *Microporous Mesoporous Mater.* 61 (2003) 199-204.
- [22] Y. Zhang, Y. Qu, D. Wang, X. C. Zeng, J. Wang, *Ind. Eng. Chem. Res.* 56 (2017) 12508-12519.
- [23] P. Aprea, B. De Gennaro, N. Gargiulo, A. Peluso, B. Liguori, F. Iucolano, D. Caputo, *Appl. Therm. Eng.* 106 (2016) 1217-1224.
- [24] V. V. Speybroeck, K. Hemelsoet, L. Joos, M. Waroquier, R. G. Bell, C. R. A. Catlow, *Chem. Soc. Rev.* 44 (2015) 7044-7111.
- [25] E. Borfecchia, K. A. Lomachenko, F. Giordanino, H. Falsig, P. Beato, A. V. Soldatov, S. Bordiga, C. Lamberti, *Chem. Sci.* 6 (2015) 548-563.
- [26] I. A. Pankin, A. Martini, K. A. Lomachenko, A. V. Soldatov, S. Bordiga, E. Borfecchia, *Catalysis Today*, 345 (2020) 125-135.
- [27] G. Beltrami, T. Chenet, L. Pasti, L. Gigli, S. Pollastri, A. Martucci, *Catalysis Today*, 345 (2020) 147-156.
- [28] G. Cametti, S. V. Churakov, *Am. Mineral.* 105 (2020) 1631-1638.
- [29] G. Cametti, *Microporous Mesoporous Mater.* 265 (2018) 162-171.
- [30] G. Cametti, A. C. Scheinost, S. V. Churakov *ACS Omega*, <http://dx.doi.org/10.1021/acsomega.0c04455>.
- [31] E. Passaglia, *Am. Mineral.* 55 (1970) 1278-1301.
- [32] CrysAlisPro, Rigaku Oxford diffraction, 2018, Version 171.40.29a.
- [33] G. M. Sheldrick, *Acta Crystallogr. A* 64 (2008) 112-122.
- [34] G. M. Sheldrick, *Acta Crystallogr. C* 71 (2015) 3-8.
- [35] K. Momma, F. Izumi, *J. Appl. Crystallogr.* 44 (2011) 1272-1276.
- [36] T. Kühne, M. Iannuzzi, M. Del Ben, V. Rybkin, P. Seewald, et al. *J. Chem. Phys.* 152 (2020) 194103.

- [37] J. Schmidt, J. VandeVondele, I. F. W. Kuo, D. Sebastiani, J. I. Siepmann, J. Hutter, C. J. Mundy, *J. Phys. Chem. B* 113 (2009) 11959-11964.
- [38] J. P. Perdew, K. Burke, M. Ernzerhof, *Phys. Rev. Lett.* 77 (1996) 3865-3868.
- [39] J. VandeVondele, J. Hutter, *J. Chem. Phys.* 127 (2007) 114105.
- [40] S. Grimme, *J. Comput. Chem.* 27 (2006) 1787-1799.
- [41] A. L. Ankudinov, B. Ravel, J.J. Rehr, S. D. Conradson, *Phys. Rev. B* 58 (1998) 7565-7576.
- [42] A. L. Ankudinov, J. J. Rehr, *Phys. Rev. B* 62 (2000) 2437-2445.
- [43] A.C. Scheinost, J. Claussner, J. Exner, M. Feig, S. Findeisen, C. Hennig, K.O.. Kvashnina, D. Naudet, D. Prieur, A. Rossberg, M. Schmidt, C. Qiu, P. Colomp, C. Cohen, E. Dettona, V.. Dyadkin, T.& Stumpf. (2020). *J. Synchrotron Rad.* In press.
- [44] S. M. Webb, *Physica Scripta* **T115** (2005) 1011-1014.
- [45] T. Ressler, *J. Synchrotron Radiation* 5 (1998) 118-122.
- [46] H. S. Sherry, *Clay Clay Miner.* 27 (1979) 231-237.
- [47] G. Cametti, A. C. Scheinost, S. V. Churakov 123 (2019) 25236-25245.
- [48] T. I. Morison, L. E. Iton, G. K. Shenoy, G. D. Stucky, S. L. Suib, *J. Chem. Phys.* 75 (1981) 4086-4089.
- [49] A. Goldbach, P. D. Barker, P. A. Anderson, P. P. Edwards, *Chemical Physics Letters* 292 (1998) 137-142.
- [50] S. B. Jang, U. S. Kim, Y. Kim, K. Seff, *J. Phys. Chem.* 98 (1994) 3796-3800.

Tables

Figures Caption

Figure 1 Crystal structure of Cd-LEV determined by SCXRD projected along [210] (a) and [100] (b). Oxygen and Si atoms are shown as blue and red spheres respectively. Fuchsia and dark cyan spheres represent Cd and Ca, respectively. Partially coloured balls display partial occupancy of atom sites. The atomic labels of the extraframework cations and water molecule are reported.

Figure 2 Snapshot of the simulated structure of Cd-LEV at 23 ps (a). Color code as in Figure 1. Al atoms and hydrogen are shown in light blue and pink, respectively. (b) Detail of the coordination of the Cd atoms to the 6DR cage of LEV. (c) Radial distribution function (RDF)

(continuous lines) and coordination number (CN) (dotted lines) of Cd-O (O = framework oxygen) and Cd-O_w (O_w = water molecules) contacts in Cd-LEV obtained from MD trajectories. Blue dotted lines are guidelines for eyes.

Figure 3 Crystal structure of Cd-ERI obtained from SC-XRD. Colour code as in Figure 1. K atoms are reported in purple.

Figure 4 (a) Snapshot of the simulated structure of Cd-ERI at 22 ps. Colour code as in Figure 2. Green dotted lines indicate the sixfold inversion-axis (b) Radial distribution function (continuous lines) and coordination number (dotted lines) of Cd-O (O = framework oxygen) and Cd-O_w (O_w = water molecules) distances in Cd-ERI obtained from MD trajectories.

Figure 5 Cd K-edge EXAFS spectra of Cd-LEV-ERI measured at 15 K, showing (a) the κ^3 -weighted $\chi(\kappa)$ function and (b) the Fourier transform magnitude and imaginary part (uncorrected for phase shift). Blue circles and red lines represent the experimental data and corresponding fits, respectively. Measured (dashed line) and fitted (continuous line) imaginary parts of the FT are also reported.

Figure 6 Radial distribution function (continuous lines) and coordination number (dotted lines) of Cd-Si and Cd-Al distances in Cd-LEV (a) and Cd-ERI (b) obtained from MD trajectories.

Figure 7 Calculated κ^3 -weighted $\chi(\kappa)$ function (continuous lines) hypothesizing 45:55 ratio of Cd-LEV and Cd-ERI obtained from (a) MD trajectories and (b) optimized structures from MD trajectories as described in section 2.5.

Figure 8 Two snapshots of the Cd-ERI structure from MD trajectories showing the Cd-coordination in the *eri* cavity. Cd²⁺ can be completely surrounded by H₂O (a) or partially linked to framework oxygen atoms (b).

Figures

Figure 1

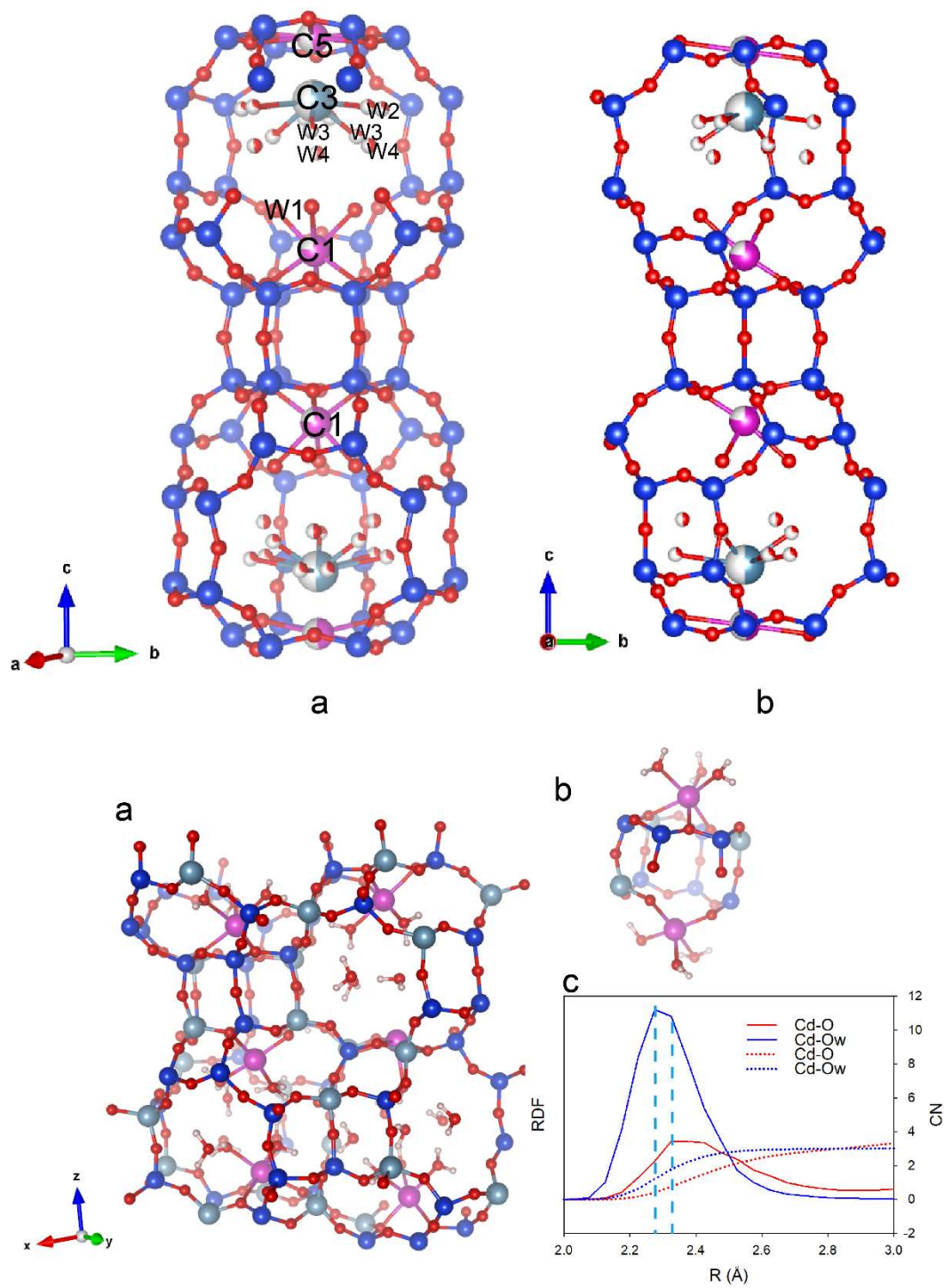


Figure 2

Figure 3

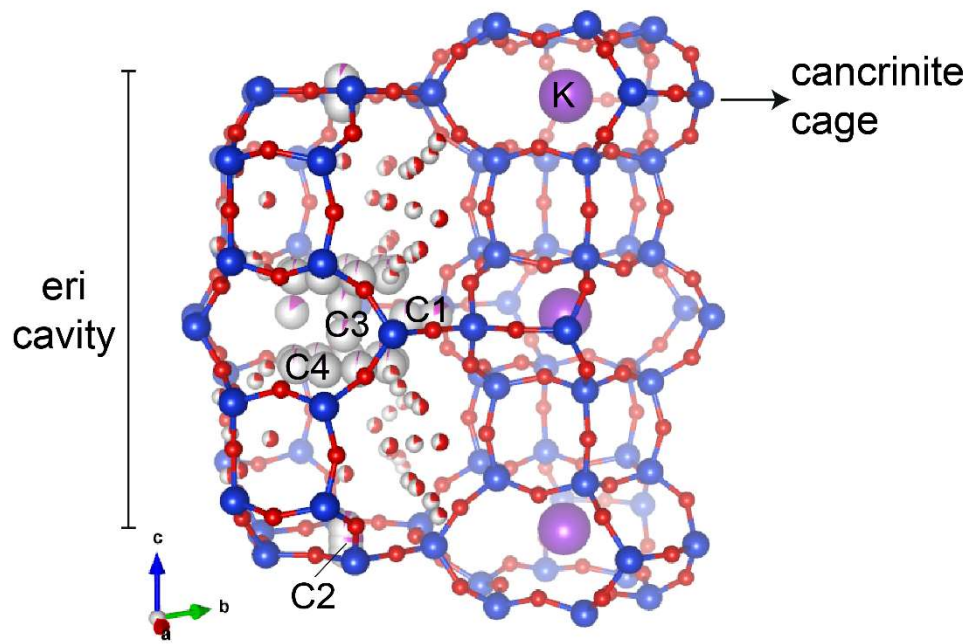


Figure 4

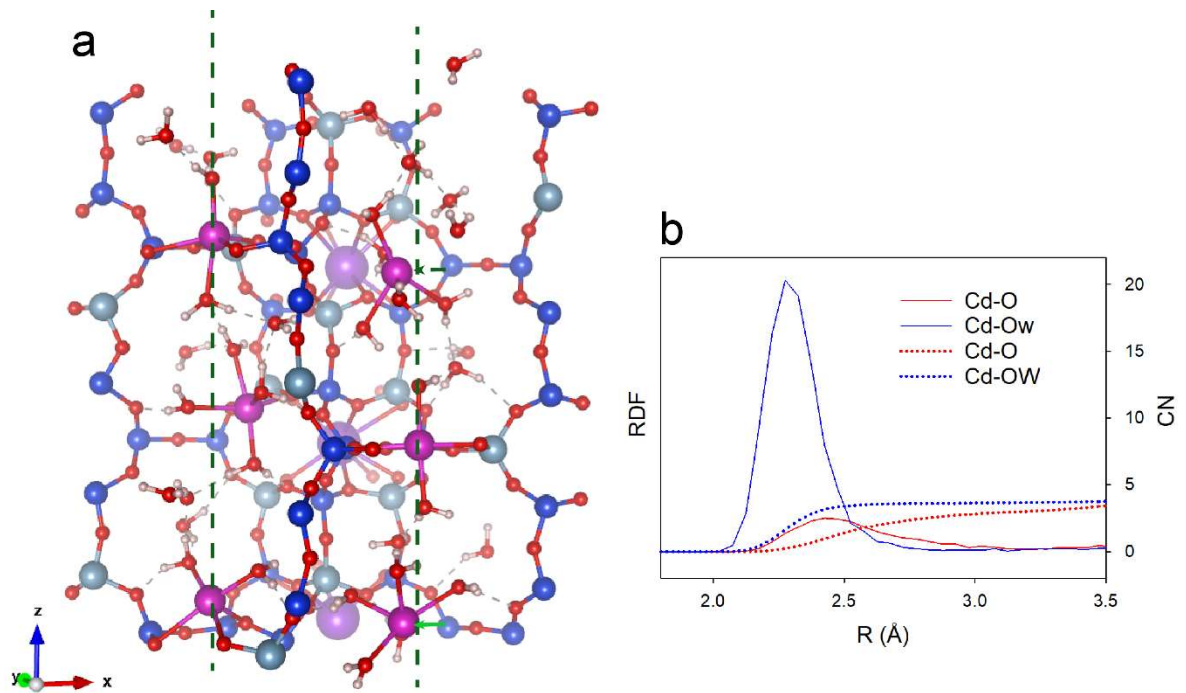


Figure 5

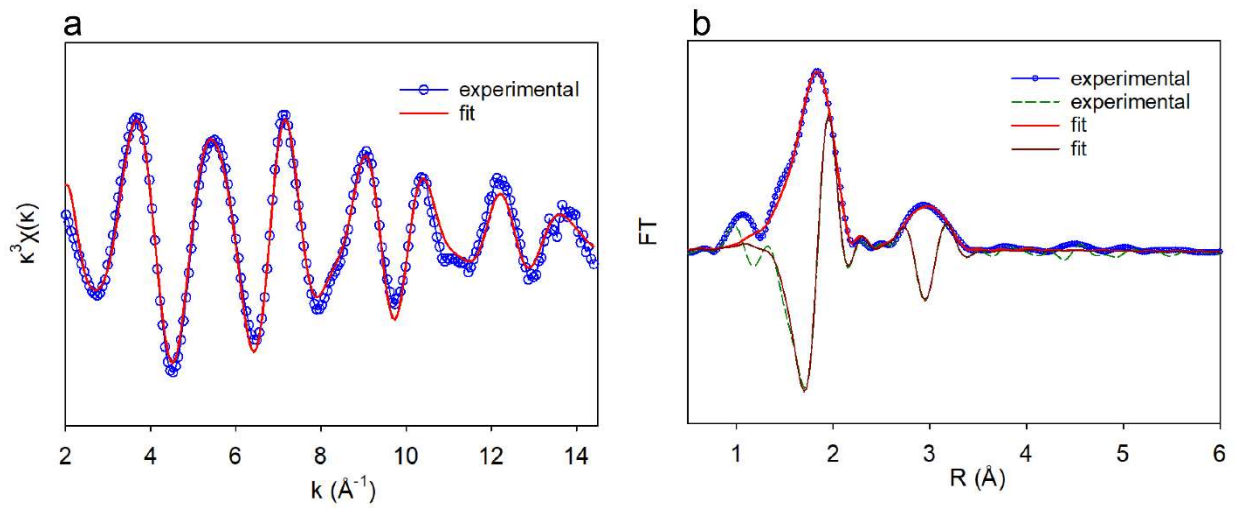


Figure 6

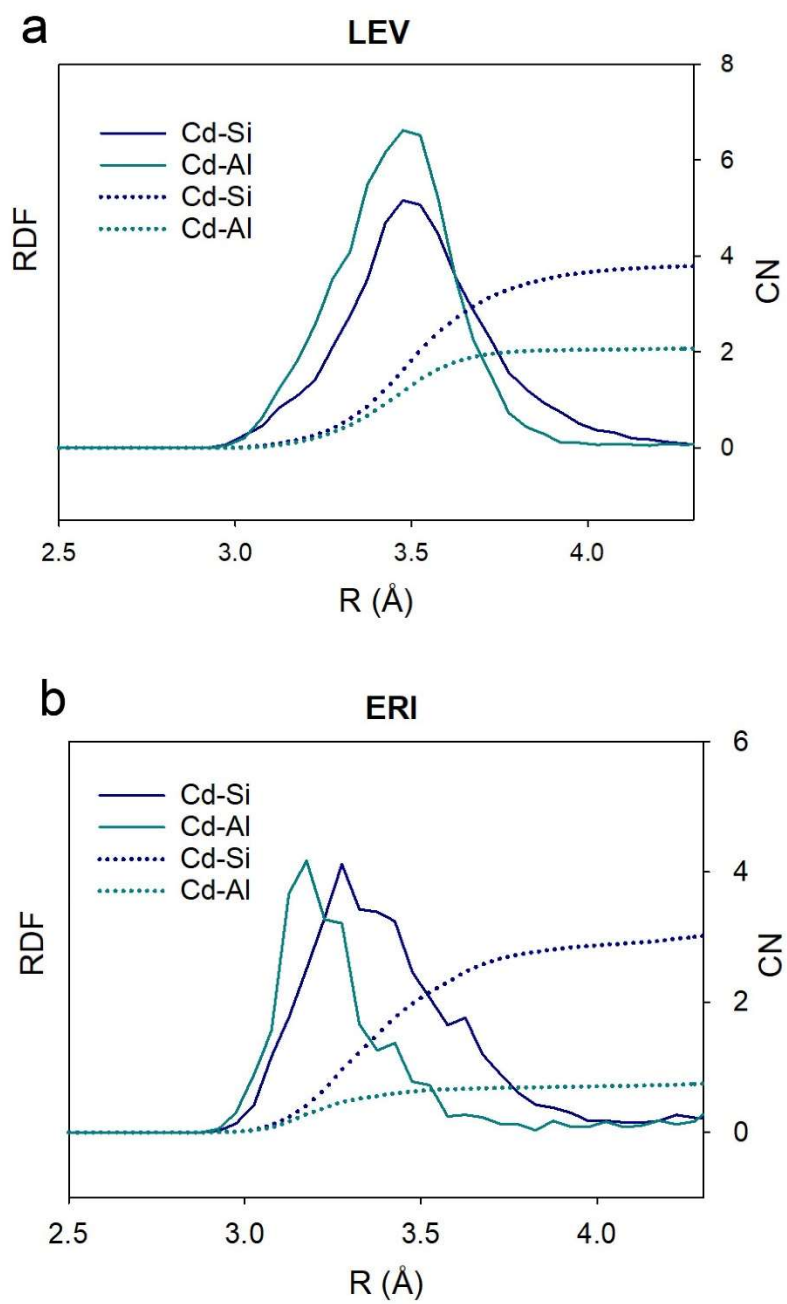


Figure 7

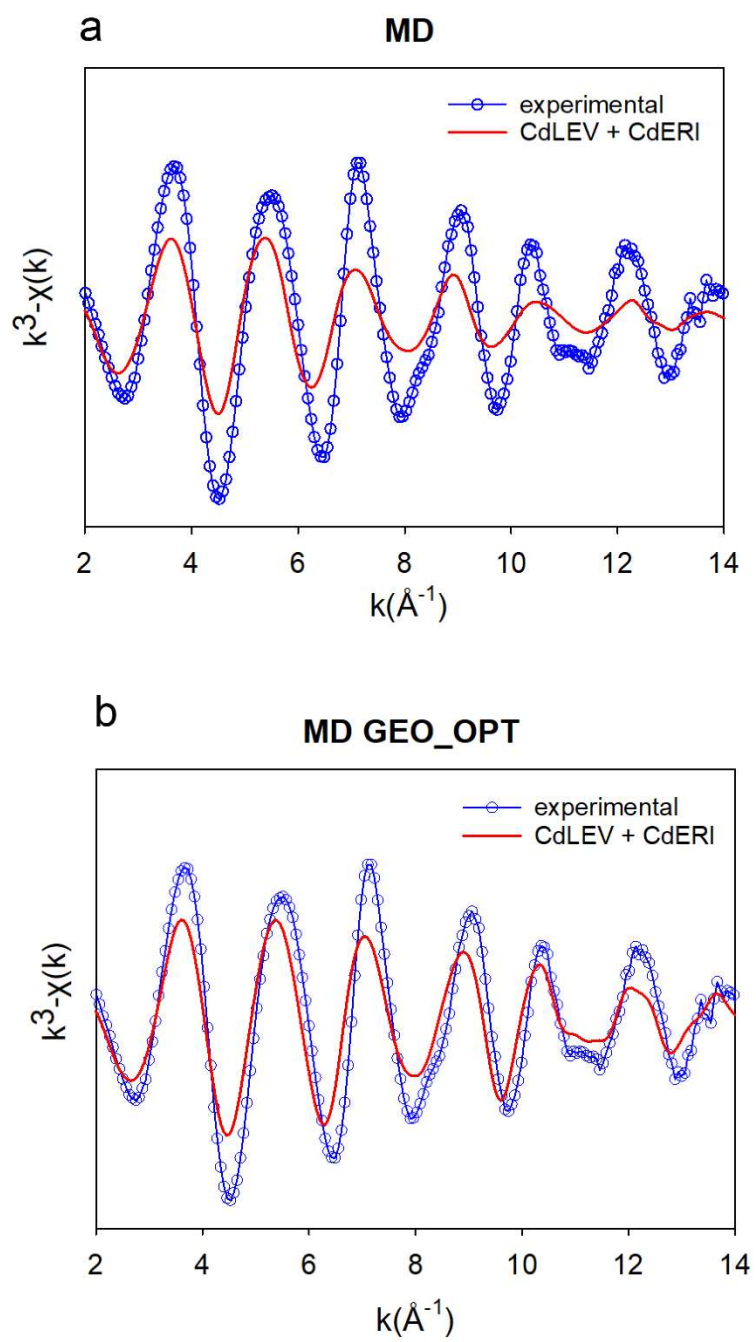


Figure 8

